

TECHNICAL NOTE

Honghua Zhao¹ and Louis Ge¹

Camera Calibration Using Neural Network for Image-Based Soil Deformation Measurement Systems

ABSTRACT: A neural network camera calibration algorithm has been adapted for image-based soil deformation measurement systems. This calibration algorithm provides a highly accurate prediction of object data points from their corresponding image points. The experimental setup for this camera calibration algorithm is rather easy, and can be integrated into particle image velocimetry (PIV) to obtain the full-field deformation of a soil model. The performance of this image-based measurement system was illustrated with a small-scale rectangular footing model. This fast and accurate calibration method will greatly facilitate the application of an image-based measurement system into geotechnical experiments.

KEYWORDS: neural network, camera calibration, particle image velocimetry

Introduction

With the rapid development in computer vision and information technology, image-based displacement/strain measurement in geotechnical testing has become feasible and popular. It provides full-field deformation data during a test instead of measuring displacements at a given location through a conventional instrumentation such as a linear variable differential transformer (LVDT). Donohoe et al. (1991) developed a system to measure soil displacements by calculating each particle's centroid during the test. The key component of their study was the edge detector technique which estimates the area and orientation for each soil particle. Hryciw and Irsyam (1993) investigated the load transfer mechanisms along the interface between sand and a ribbed plate. A direct shear box was constructed with Plexiglass walls so that a video camera could be used to observe and measure sand particle displacements. Guler et al. (1999) adapted two techniques (MATCH and BMAD) to determine soil particle displacement vectors using the images from direct shear tests. Paikowsky and Xi (2000) used a high-resolution digital CCD camera to track an assembly of two-dimensional disks in an interfacial friction shear box. Image-based deformation measurement systems have also been applied to monitor and analyze shear band formation. Alshibli and Sture (2000) conducted a series of plane strain experiments on sands. A grid pattern was imprinted on the latex membrane for each specimen and images were taken to analyze a shear band formation analyses. Without using markers on the latex membrane, Rechenmacher and Finno (2003) also performed plane strain experiments on dense sands and used digital image correlation to quantify shear band inclination and thickness. Aydilek et al. (2004) implemented a block-based matching image algorithm to obtain the strain distribution in geosynthetics during tensile testing. In geotechnical centrifuge testing, Allersma (1991)

demonstrated the use of an image processing technique to monitor the progressive failure of a clay slope model during flight. Taylor et al. (1998) developed a system for measuring planar and three-dimensional surface movement in centrifuge tunnel heading experiments to investigate stability and collapse mechanisms. White et al. (2003, 2005) adapted particle image velocimetry (PIV) and close-range photogrammetry to create a soil deformation measurement system which was developed for centrifuge testing. The illustrated examples include the installation of a displacement pile, the progressive failure of a model clay embankment, and the deformation patterns beneath an eccentrically-loaded plane strain strip foundation on clay.

Camera Calibration

In the application of image-based deformation measurement to geotechnical experiments, the performance of the system depends on the image analysis method that is used to determine the correlation between the image and object coordinates or that tracks soil particles during a test (White et al. 2003). Camera calibration is an important component of an image-based measurement system. Its goal is to link a point $P(X, Y)$ in the object coordinate system to the corresponding point $p(u, v)$ in the image plane coordinate system, as depicted in Fig. 1.

The simplest way to do camera calibration is through the pin-hole camera method, which is based on the principle of collinearity (Heikkila and Silven 1997). A linear relation between an object point and its image point is assumed. Due to the fact that the camera lens distorts images and also because the object is commonly behind a refractive window, a simple relation between the object points and the image points does not normally exist. Taylor et al. (1998) first applied close range photogrammetry in centrifuge modeling. In their camera calibration model, nine parameters are needed, including two orthogonal offsets between the center of the CCD array and the intersection of the optical axis of the camera with the array, the focal length of the camera, three polynomial co-

Manuscript received July 16, 2006; accepted for publication August 3, 2007; published online October 2007.

¹Civil, Architectural, and Environmental Engineering, University of Missouri-Rolla, 1870 Miner Circle, MO 65409

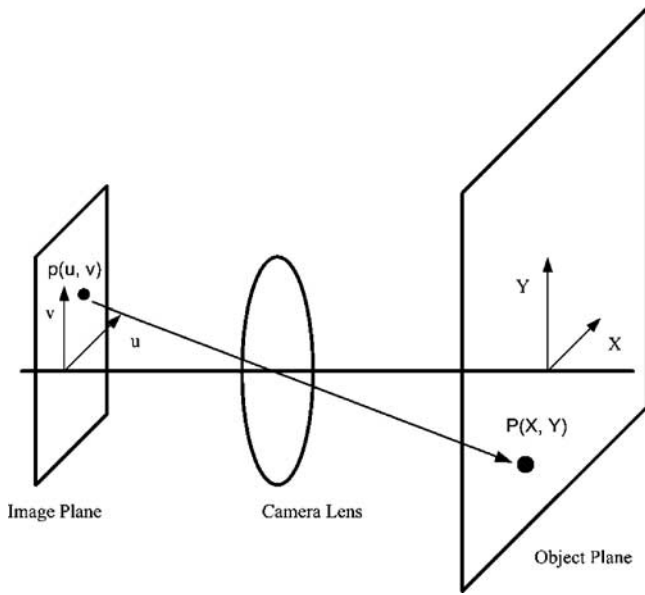


FIG. 1—Concept of camera calibration.

efficients representing radial geometric lens distortions, two polynomial coefficients corresponding to tangential geometric lens distortions, and a differential scale parameter in the image to account for the nonsquare pixels. This nine-parameter model can correct image distortions such as fisheye and barreling. Paikowsky and Xi (2000) used a steel plate with 121 evenly distributed 4.76-mm diameter points, 50 mm apart as the calibration object points. A polynomial function was used to fit points in the object plane to the image plane. The absolute error could reach 0.4 mm. Recently, White et al. (2003) have implemented the 14-parameter model of Heikkila and Silven (1997) to perform camera calibration for their image-based deformation measurement system in centrifuge experiments.

The Camera Calibration Toolbox for Matlab developed by Bouquet (2006) at Caltech was used as a framework for the current research. The features of the toolbox include loading calibration images, extracting image corners, running the calibration engine, displaying the results, controlling accuracies, etc. A neural network-based calibration method was proposed and implemented into the Toolbox. The method was then examined by the calibration data for measuring the planar deformation of soils. An example of this calibration algorithm integrated with PIV code MatPIV (Sveen 2004) was illustrated with a rectangular footing model. The image acquiring system used in this research is the Light Wise LW-1.3-G-1394 digital camera from Image Solution Group, which has a resolution of 1280 by 1024 pixels. It is noted, however, that this method does not give images containing both the soil under observation and also the calibration points. If the camera or test model container moves between calibration and the experiment, the calibration is invalid. This can be improved by using a method with concurrent soil and control point data (Taylor et al. 1998; White et al. 2003).

Neural Network Calibration Model

The neural network trained in this study is a three-layer, feed-forward neural network (2–15–2 NN). The input layer consists of $n_1=2$ input nodes, and the output layer consists of $n_2=2$ output

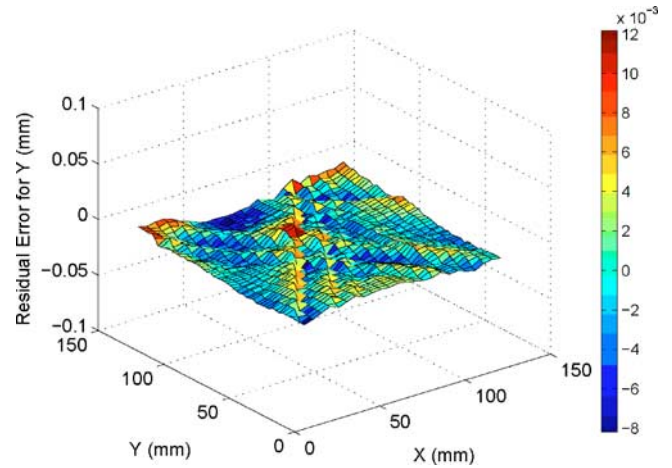


FIG. 2—Residual error for X from the neural network model.

nodes. The hidden layer consists of 15 neurons. Input data are the image points $p(u, v)$ obtained from the extraction of the corner points. The target data are the corner points $P(X, Y)$ from the calibration plane, and the training data are from half of the calibration points. The other half of the calibration data is used as testing data to test the neural network. A total of 2500 data points were used in this study with 2.5 mm separation distance between two neighbor points. This gives a field of view (FOV) of 145 mm by 155 mm.

The neural network training algorithm used was a back-propagation function, which updates the weight and bias values according to Levenberg-Marquardt optimization method. In the training process, the input layer takes an input vector of size $n_1=2$ and passes it to the hidden layer. Next, the hidden layer maps this input vector to a vector of size $n_3=2$ by a tangent sigmoid transfer function $\text{tansig}(\zeta)$:

$$a = \frac{2}{1 + e^{-2\zeta}} - 1 \quad (1)$$

where ζ is an activation function, the sum of the weighted inputs and biases. This vector from the hidden layer is then mapped by a pure linear transfer function to an output layer. The performance of the neural network model is defined by the normalized square error MSE, expressed as

$$MSE = \frac{1}{2QN} \sum_{q=1}^Q \sum_{h=1}^N (d_{qh} - x_{out,qh})^2 \quad (2)$$

where Q is the number of outputs, N is the total number of data sets, d_{qh} is the set of target data; $x_{out,qh}$ is the set of network output data. To determine the appropriate number of neurons in the hidden layer, different numbers of neurons (5, 10, 15, and 20) were tested. It was found that 15 neurons in the hidden layer gave the best performance.

Neural Network Model Validation

The proposed neural network calibration model was verified through the testing data, which were not used in the training process. The maximum absolute residual errors for X and Y coordinates were 0.011 mm (1/13182 of FOV) and 0.014 mm (1/11071 of FOV), respectively. The residual errors for X and Y are shown in Figs. 2 and 3, respectively. It is clear from Figs. 2 and 3 that the

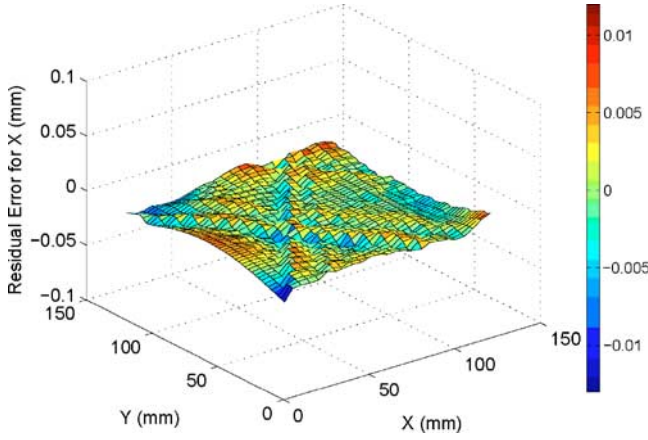


FIG. 3—Residual error for Y from the neural network model.

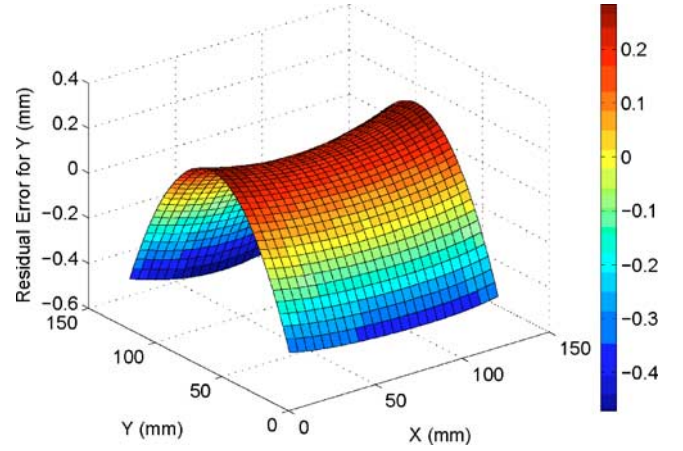


FIG. 5—Residual error for Y from the linear calibration model.

residual error is small and distributed uniformly throughout the entire calibration area.

Comparison with Other Calibration Algorithms

To examine the effectiveness of this neural network model, the linear and second-order polynomial calibration algorithms were also studied in this research, which are expressed in Eqs. 3 and 4:

$$\begin{cases} X = a_1 + a_2u + a_3v \\ Y = b_1 + b_2u + b_3v \end{cases} \quad (3)$$

$$\begin{cases} X = a_1 + a_2u + a_3v + a_4u^2 + a_5v^2 + a_6uv \\ Y = b_1 + b_2u + b_3v + b_4u^2 + b_5v^2 + b_6uv \end{cases} \quad (4)$$

where X, Y are the coordinates of point P in the object plane; u, v are the coordinates of corresponding image point p in the image plane; and a_i, b_i are the coefficient for the model. The coefficients a_i, b_i were determined from the normalized least square method using the same training data as used for the neural network model. These models were also tested using the same testing data to examine their prediction accuracy. Figures 4 and 5 show the residual error for X and Y from the linear calibration model, respectively. The residual error is small in the center of the calibration plane and becomes large towards the edges of the calibration plane. Figure 6 shows the residual error for Y from the linear calibration model.

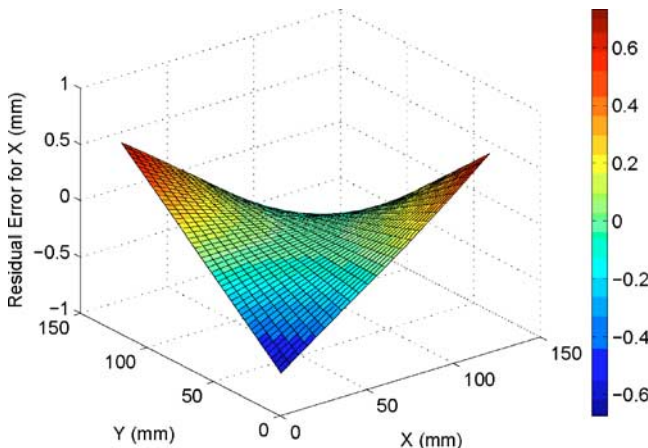


FIG. 4—Residual error for X from the linear calibration model.

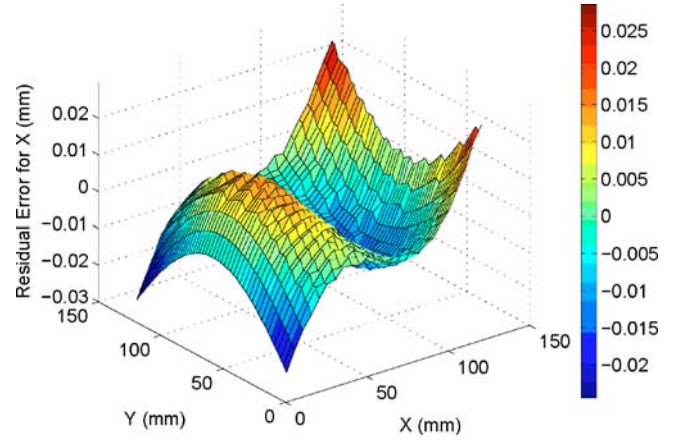


FIG. 6—Residual error for X from the second-order polynomial model.

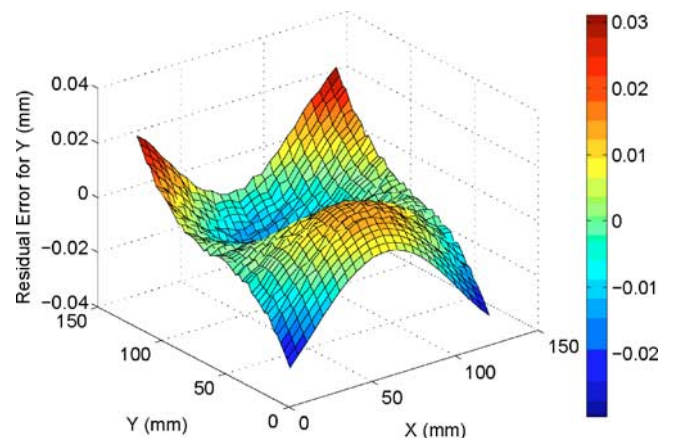


FIG. 7—Residual error for Y from the second-order polynomial model.

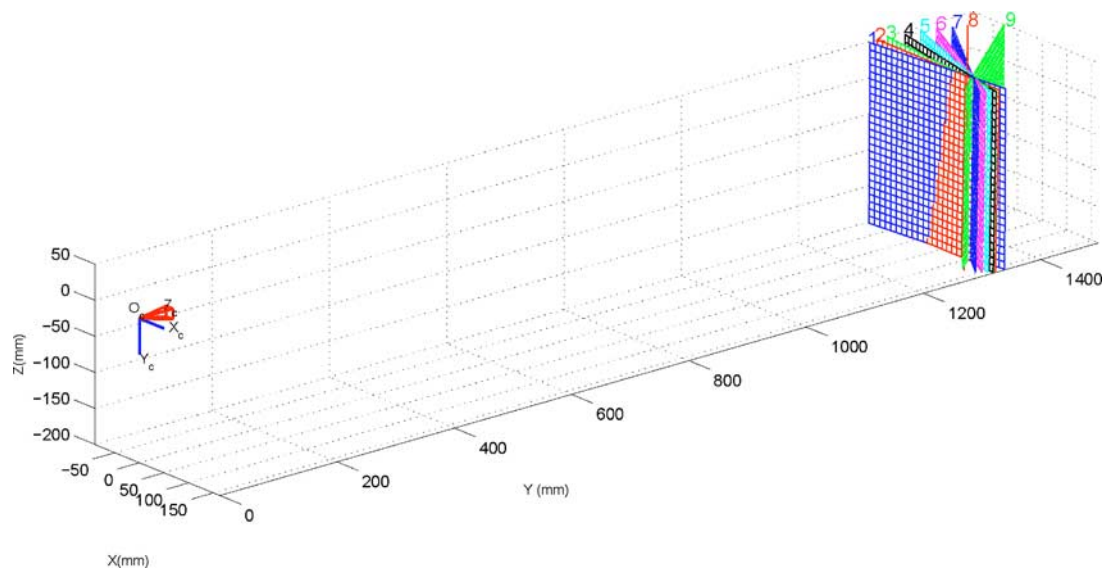


FIG. 8—Different calibration planes for angle error analysis.

rotating by 90° . Both have a larger error at the four corners of the plane and a smaller error at the center area of the calibration plane. The maximum absolute residual error is 0.672 mm (1/215 of FOV) for X and 0.685 mm (1/266 of FOV) for Y from the linear calibration algorithm. The maximum absolute residual error is 0.030 mm (1/4833 of FOV) for X and 0.032 mm (1/4844 of FOV) for Y from the second-order polynomial algorithm. These values are much higher than those errors from the neural network calibration algorithm.

Angle Error Analysis

The effects of the angle (θ) between the calibration plane and the image sensor plane on the residual error were also investigated. In the setup for this experiment, first the calibration plane was closely aligned to the image sensor plane; then, the calibration plane was rotated to different angles (θ), as shown in Fig. 8. Images of the calibration plane were taken by the camera while keeping the position of the camera fixed during this process. Table 1 shows the residual errors obtained from the neural network model, the linear calibration model, and the second-order polynomial model for each

calibration plane. From Table 1, it is evident that the linear algorithm gives the largest absolute residual error among the three different calibration methods.

When the angle, θ , is small, the second-order polynomial model can predict the data well. However, the error increases as the angle becomes larger. The neural network calibration algorithm was found to perform the best, because it gives the minimum absolute residual error, and also the error does not vary much as the angle increases.

Application of the Calibration Algorithm in Particle Image Velocimetry

A small-scale wood block (6.35 cm by 7.62 cm by 15.88 cm) was placed on top of the sand in a model container (35.56 cm by 6.60 cm by 35.56 cm), as shown in Fig. 9. The height of the sand was 18.92 cm (7.45 in.), and a loading frame was used to apply the vertical load to the foundation. The camera was set up to take images of the soil below the footing during the loading. The loading rate was set to 2.54 mm/min (0.1 in./min). The test setup is illus-

TABLE 1—Absolute error for nine planes from the three calibration algorithms.

Plane No.	Angle θ ($^\circ$)	Maximum Absolute Residual Error					
		Linear Model		Second-Order Polynomial Model		Neural Network Model	
		mm	Fraction Of FOV	mm	Fraction of FOV	mm	Fraction of FOV
1	7.62	0.672	1/215	0.030	1/4833	0.014	1/11071
2	13.61	1.499	1/97	0.044	1/3295	0.025	1/5800
3	17.97	1.932	1/75	0.057	1/2544	0.016	1/9063
4	25.60	1.932	1/75	0.095	1/1526	0.039	1/3718
5	30.87	3.348	1/43	0.130	1/1115	0.038	1/3816
6	36.49	3.944	1/37	0.199	1/729	0.014	1/10357
7	39.43	4.427	1/33	0.202	1/718	0.016	1/9063
8	50.66	4.482	1/32	0.274	1/529	0.056	1/2589
9	53.93	4.722	1/31	0.303	1/479	0.062	1/2339

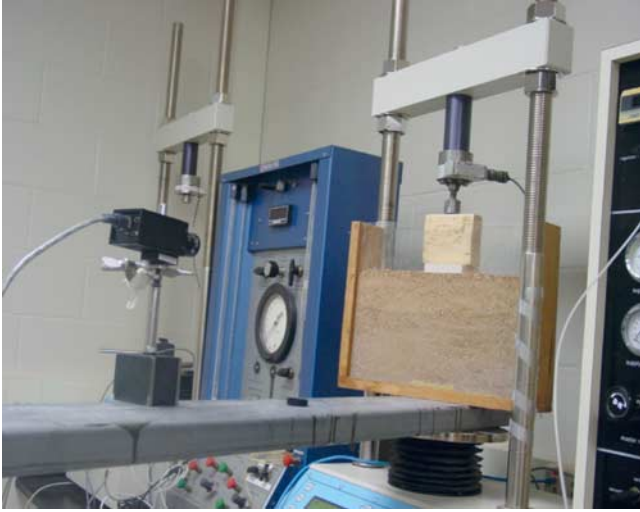
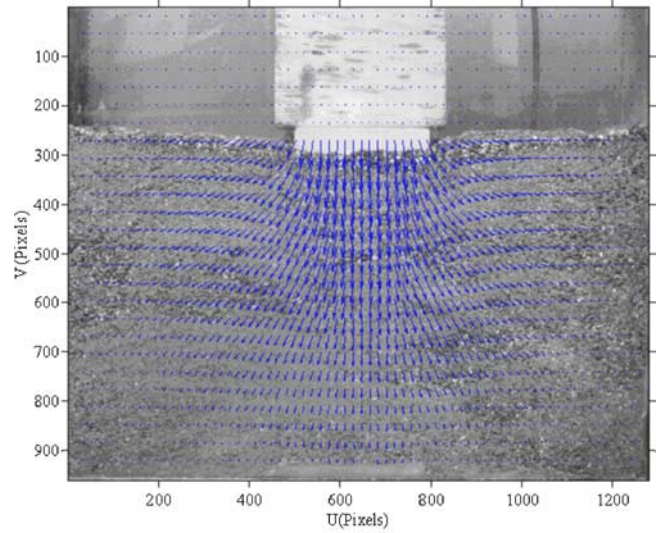


FIG. 9—Experiment setup for the rectangular footing model.

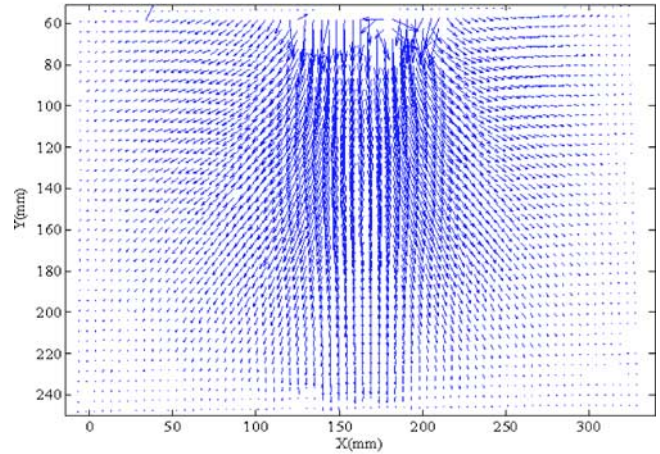
trated in Fig. 10. A long steel plate was put on the loading platen of the frame, the sand box rested on the steel plate, and the digital camera was set about 2 m from the sand box at the other end of the steel plate. This setup ensured that the digital camera was moving together with the loading platen during the loading process. Images were taken every 30 seconds. The proposed neural network camera calibration algorithm was implemented into MatPIV, a computer code initially developed by Svein (2004) for PIV, to process the images. The principles behind PIV are image pattern matching techniques. Assume two images (I_1 and I_2) are obtained, and these two images are divided into smaller regions (subwindows, interrogation-windows, or interrogation-regions). Then, each subwindow in the image, I_1 , is compared with the corresponding subwindow in the image, I_2 . The cross-correlation between the two subwindows is defined as

$$R(s,t) = \sum_{m=0}^{M-1} \sum_{n=0}^{N-1} I_1^{i,j}(m,n) \times I_2^{i,j}(m-s,n-t) \quad (5)$$

where $I_1^{i,j}$ is the subwindow number (i,j) in the first image, I_1 ; and $I_2^{i,j}$ is the subwindow number (i,j) in the second image, I_2 . When this expression reaches its peak value, the two subwindows will most likely match each other. The subwindow has moved s and t units in i and j directions, respectively. By a centroid fit, a Gaussian fit, or a parabolic fit to the region close to the peak, the system can achieve subpixel resolution. The smallest window size used in this analysis was 36 pixels by 36 pixels in order to cover the large displacement of sand particles. The digital image correlation method was applied to analyze the two images to obtain the full-field deformation of the soil surrounding the footing. Figures 10(a) and 10(b) show the displacement vector field of the soil under the footing at $t=6$ min, and $P=0.92$ kN (20.6 lb), which are similar to cylindrical cavity expansion. Therefore, Figs. 11(a) and 11(b) show circular contours of displacement. From the experimental results, no Terzaghi's failure mechanism was observed, i.e., the vertical movement extends to too great a depth to match Terzaghi's mechanism, and there is no heave beside the footing as predicted by Terzaghi.



(a)



(b)

FIG. 10—(a) Deformation vector field of sand under the rectangular footing in the image space ($t=6$ min, $P=0.92$ kN). (b) Deformation vector field of sand under the rectangular footing in the object space ($t=6$ min, $P=0.92$ kN).

Conclusions

A three-layer back-propagation neural network calibration algorithm was developed for camera calibration in an image-based measurement system. This algorithm was compared with the linear calibration and second-order polynomial calibration algorithms. When the angle between the image plane and object plane became large, the linear calibration algorithm and second-order polynomial calibration algorithm gave a considerable error. It was found that the neural network calibration model will give a very accurate result independent of the angle between the image plane and the object plane. This algorithm can be easily integrated into MatPIV to obtain the full-field deformation of the soil below the footing. This fast and accurate calibration method will greatly facilitate the application of an image-based measurement system into geotechnical experiments.

Acknowledgment

This work was partially supported by funds from the University of Missouri Research Board. The comments and suggestions from the manuscript reviewers is also greatly acknowledged.

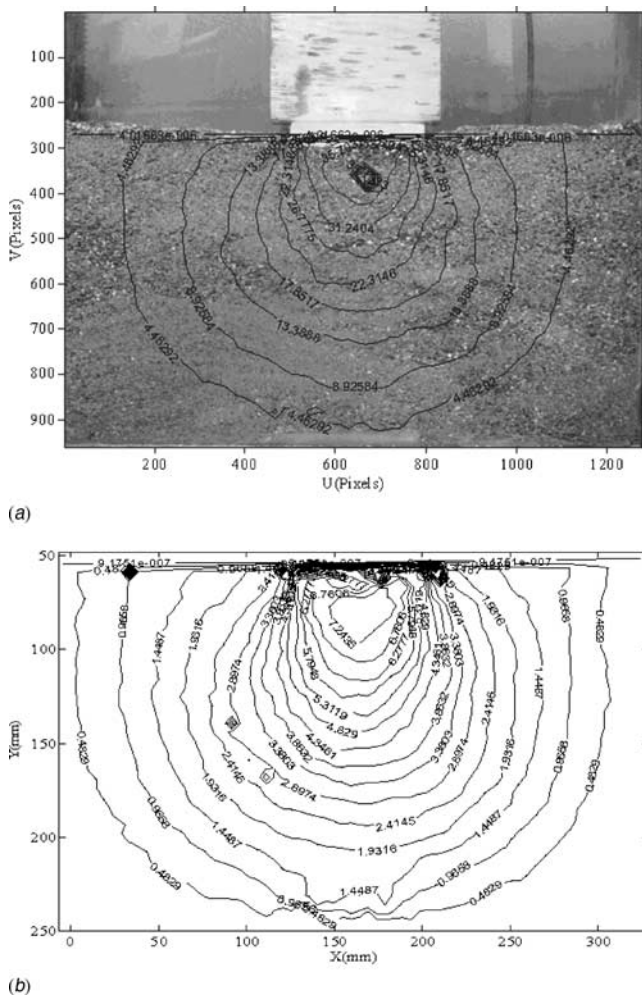


FIG. 11—(a) Magnitude contour of displacement vector for sand under the rectangular footing in the image space (contour label in unit of pixels, $t = 6$ min, $P = 0.92$ kN). (b) Magnitude contour of displacement vector for sand under the rectangular footing in the object space (contour label in unit of mm, $t = 6$ min, $P = 0.92$ kN).

References

- [1] Allersma, H. G. B., 1991, "Using Image Processing in Centrifuge Research," *Proceedings, Centrifuge '91*, Colorado, Balkema, pp. 551–559.

- [2] Alshibli, K. A., and Sture, S., 2000, "Shear Band Formation in Plane Strain Experiments of Sand," *J. Geotech. Geoenviron. Eng.*, Vol. 126, No. 6, pp. 495–503.
- [3] Aydilek, A. H., Guler, M., and Edil, T. B., 2004, "Measurement of Particle Movement in Granular Soils Using Image Analysis," *J. Comput. Civ. Eng.*, Vol. 18, No. 1, pp. 65–74.
- [4] Bouguet, J.-Y., 2006, Camera Calibration Toolbox for Matlab, Computer Vision Research Group, Department of Electrical Engineering, California Institute of Technology, http://www.vision.caltech.edu/bouguetj/calib_doc/index.html.
- [5] Donohoe, G. W., Bacabella, M. F., and Gill, J. J., 1991, "Segmentation and Object Tracking for the Microstructure Analysis of Soil," *IEEE Conference on Signals, Systems and Computers*, Pacific Grove, CA, 2, pp. 1215–1219.
- [6] Guler, M., Edil, T. B., and Bosscher, P. J., 1999, "Measurement of Particle Movement in Granular Soils Using Image Analysis," *J. Comput. Civ. Eng.*, Vol. 13, No. 2, pp. 116–122.
- [7] Heikkila, J., and Silven, O., 1997, "A Four-Step Camera Calibration Procedure with Implicit Image Correction," *IEEE Computer Society Conference on Computer Vision and Pattern Recognition (CVPR '97)*, San Juan, Puerto Rico, pp. 1106–1112.
- [8] Hryciw, R. D., and Irsyam, M., 1993, "Behavior of Sand Particles Around Rigid Ribbed Inclusions During Shear," *Soils Found.*, Vol. 33, No. 3, pp. 1–13.
- [9] Paikowsky, S. G., and Xi, F., 2000, "Particle Motions Tracking Utilizing a High-Resolution Digital CCD Camera," *Geotech. Test. J.*, Vol. 23, No. 1, pp. 123–134.
- [10] Rechenmacher, A. L., and Finno, R. J., 2004, "Digital Image Correlation to Evaluate Shear Banding in Dilative Sands," *Geotech. Test. J.*, Vol. 27, No. 1, pp. 1–10.
- [11] Sveen, J. K., 2004, An Introduction to MatPIV, v.1.6.1. Eprint No.2, ISSN 0809-4403, Dept. of Math., University of Oslo.
- [12] Taylor, R. N., Grant, R. J., Robson, S., and Kuwano, J., 1998, "An Image Analysis System for Determining Plane and 3-D Displacements in Soil Models," *Proceedings, Centrifuge '98*, Tokyo, pp. 73–78.
- [13] White, D., Randolph, M., and Thompson, B., 2005, "An Image-Based Deformation Measurement System for the Geotechnical Centrifuge," *International Journal of Physical Modelling in Geotechnics*, Vol. 5, No. 3, pp. 1–12.
- [14] White, D. J., Take, W. A., and Bolton, M. D., 2003, "Soil Deformation Measurement Using Particle Image Velocimetry (PIV) and Photogrammetry," *Geotechnique*, Vol. 53, No. 7, pp. 619–631.